RSC Advances

PAPER

View Article Online
View Journal | View Issue

Cite this: *RSC Adv.*, 2016, **6**, 33951

Tuning the high-temperature properties of $Pr_2NiO_{4+\delta}$ by simultaneous Pr- and Ni-cation replacement†

S. Ya. Istomin,*[a] O. M. Karakulina,[a] M. G. Rozova,[a] S. M. Kazakov,[a] A. A. Gippius,[ab] E. V. Antipov,[a] I. A. Bobrikov,[c] A. M. Balagurov,[c] A. A. Tsirlin,[de] A. Michau,[f] J. J. Biendicho[fgh] and G. Svensson[f]

Novel $Pr_{2-x}Sr_xNi_{1-x}Co_xO_{4\pm\delta}$ (x = 0.25; 0.5; 0.75) oxides with the tetragonal K_2NiF_4-type structure have been prepared. Room-temperature neutron powder diffraction (NPD) study of x = 0.25 and 0.75 phases together with iodometric titration results have shown the formation of hyperstoichiometric oxide for x = 0.25 (δ = 0.09(2)) and a stoichiometric one for x = 0.75. High-temperature X-ray powder diffraction (HT XRPD) showed substantial anisotropy of the thermal expansion coefficient (TEC) along the a- and c-axis of the crystal structure, which increases with increasing the Co content from TEC(c)/TEC(a) = 2.4 (x = 0.25) to 4.3 (x = 0.75). High-temperature NPD (HT NPD) study of the x = 0.75 sample reveals that a very high expansion of the axial (Ni/Co)–O bonds (75.7 ppm K^{-1} in comparison with 9.1 ppm K^{-1} for equatorial ones) is responsible for such behaviour, and is caused by a temperature-induced transition between low- and high-spin states of Co^{3+}. This scenario has been confirmed by high-temperature magnetization measurements on a series of $Pr_{2-x}Sr_xNi_{1-x}Co_xO_{4\pm\delta}$ samples. For compositions with high Ni content (x = 0.25 and 0.5) we synthesised K_2NiF_4-type oxides $Pr_{2-x-y}Sr_{x+y}(Ni_{1-x}Co_x)O_{4\pm\delta}$, y = 0.0–0.75 (x = 0.25); y = 0.0–0.5 (x = 0.5). The studies of the TEC, high-temperature electrical conductivity in air, chemical stability of the prepared compounds in oxygen and toward interaction with $Ce_{2-x}Gd_xO_{2-x/2}$ (GDC) at high temperatures reveal optimal behaviour of $Pr_{1.35}Sr_{0.65}Ni_{0.75}Co_{0.25}O_{4+\delta}$. This compound shows stability in oxygen at 900 °C and does not react with GDC at least up to 1200 °C. It features low TEC of 13 ppm K^{-1} and high-temperature electrical conductivity in air of 280 S cm^{-1} at 900 °C, thus representing a promising composition for use as a cathode material in intermediate temperature solid oxide fuel cells (IT-SOFC).

Received 2nd February 2016
Accepted 25th March 2016

DOI: 10.1039/c6ra03099h

www.rsc.org/advances

Introduction

Layered nickelates $R_2NiO_{4+\delta}$ (R = La, Pr, Nd) have been considered as promising cathode materials for intermediate temperature (750–900 °C) solid oxide fuel cells (IT-SOFC) due to their high electrical conductivity, fast oxygen diffusion and thermal expansion coefficient (TEC) compatible with typical SOFC electrolytes.[1] The crystal structure of these nickelates belongs to the K_2NiF_4 type and consists of alternate rock-salt and perovskite slabs (Fig. 1). Due to a size mismatch between metal–oxygen distances of Ni^{2+} and rare earth cations, the NiO_6 octahedra tilt, which results in a lowering of the crystal structure symmetry from tetragonal (ideal K_2NiF_4-type structure) to orthorhombic.[2,3] Incorporation of extra oxygen atoms (δ), occupying the tetrahedral voids in the rock-salt slab (Fig. 1) reduces this mismatch due to a decrease of the nickel ionic radius caused by partial oxidation of Ni^{2+} to Ni^{3+}.[4–6] The amount of hyperstoichiometric oxygen δ depends on the rare-earth cation (R). The smaller the radius of the R cations, the higher the oxygen content (R = La, δ = 0.16;[7] R = Pr, Nd, δ = 0.21–0.23 (ref. 5, 6 and 8)) for phases synthesized at the same conditions. The hyperstoichiometric oxygen atoms can diffuse by an interstitial mechanism within the rock-salt slab of the K_2NiF_4-type structure involving as well apical oxygen atoms.[9] This results in higher oxygen diffusion in rare-earth nickelates $R_2NiO_{4+\delta}$ (R = La, Pr, Nd) in comparison with traditional IT-SOFC cathode material like (La,Sr)(Co,Fe)$O_{3-\delta}$ (LSFC), with the perovskite structure. The highest oxygen diffusion (D^* = 2.5 × 10^{-8}

[a]*M.V. Lomonosov Moscow State University, Moscow 119991, Russia. E-mail: istomin@icr.chem.msu.ru*
[b]*A.V. Shubnikov Institute of Crystallography, Moscow 117333, Russia*
[c]*Joint Institute for Nuclear Research, Dubna 141980, Russia*
[d]*National Institute of Chemical Physics and Biophysics, 12618 Tallinn, Estonia*
[e]*Experimental Physics VI, Centre for Electronic Correlations and Magnetism, University of Augsburg, 86159 Augsburg, Germany*
[f]*Department of Materials and Environmental Chemistry, Stockholm University, S-106 91 Stockholm, Sweden*
[g]*The ISIS Facility, STFC Rutherford Appleton Laboratory, Didcot OX110 QX, Oxfordshire, UK*
[h]*IREC, Catalonia Institute for Energy Research, Jardins de les Dondes de Negre, e1, 08930 Sant Adria del Besos, Spain*

† Electronic supplementary information (ESI) available: Results of the refinement of the crystal structures using NPD data. See DOI: 10.1039/c6ra03099h

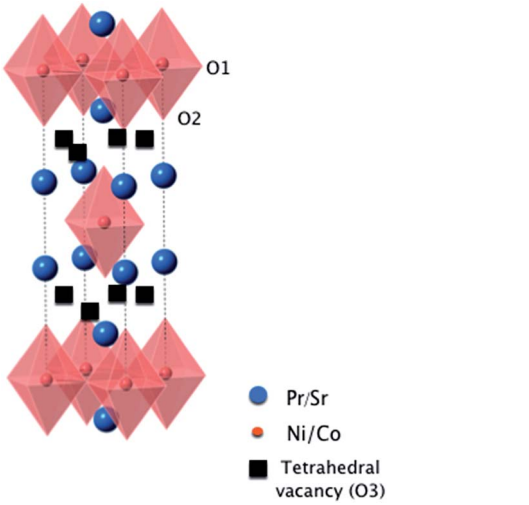

Fig. 1 The crystal structure of $(Pr,Sr)_2(Ni,Co)O_{4+\delta}$ (K_2NiF_4-type). Hyperstoichiometric oxygen atoms (δ) are located in the tetrahedral vacancies.

$cm^2\ s^{-1}$) and surface exchange ($k = 5 \times 10^{-7}$ cm s^{-1}) coefficients at 600 °C have been observed in $Pr_2NiO_{4+\delta}$.[1] Other advantages of $Pr_2NiO_{4+\delta}$ are the highest electrical conductivity among other rare-earth nickelates and low TEC. However, it is unstable in oxygen in comparison with $La_2NiO_{4+\delta}$ and $Nd_2NiO_{4+\delta}$ and decomposes with the formation of $Pr_4Ni_3O_{10}$ and Pr_6O_{11} at 850 °C.[10]

Both crystal structure and high-temperature properties of R_2NiO_4 oxides can be modified by cation substitution in the A- and B-sublattices. Partial replacement of rare-earth cations by larger Sr^{2+} according to the chemical formula $R_{2-x}Sr_xNiO_{4+\delta}$ resulted in the formation of solid solutions with tetragonal K_2NiF_4 structure. A solid solution with tetragonal symmetry is observed for $x = 0.2$–1.0 for R = La,[11] Pr,[7] Nd,[12] and from 0.8 to 1.0 for Sm.[7] The increase of Sr content is accompanied by a decrease of the hyperstoichiometric oxygen content giving rise to oxygen-deficient phases. The range of x in which δ is negative is not well defined and varies depending upon the synthesis conditions.[8,13,14] The TEC drastically increases with increasing of Sr-content up to 16 ppm K^{-1} for $LaSrNiO_{4+\delta}$.[15] Meanwhile, high-temperature electrical conductivity increases reaching 273 S cm^{-1} at 600 °C for $x = 0.75$. A similar trend is observed for $Pr_{2-x}Sr_xNiO_{4+\delta}$, where the conductivity is higher than 100 S cm^{-1} for the substituted phases ($x \geq 0.5$).[16,17] The oxygen diffusion coefficient D^* is the highest for unsubstituted $La_2NiO_{4+\delta}$ and decreases with increasing the Sr-content.[18,19] However, recently an increase of D^* has been observed for compositions with high amount of Sr ($x = 0.8$).[19]

With the aim to improve the chemical stability in oxygen, high-temperature electrical conductivity and electrocatalytic activity of $R_2NiO_{4+\delta}$ for oxygen reduction in the present work we introduced Co^{3+} cations in $Pr_2NiO_{4+\delta}$. This was performed by the simultaneous replacement of the equal amounts of Pr and Ni cations by Sr and Co, respectively, according to the chemical formula $Pr_{2-x}Sr_xNi_{1-x}Co_xO_{4\pm\delta}$ ($x = 0.25$; 0.5; 0.75; 1.0). For compositions with high Ni-content ($x = 0.25$ and 0.5) we synthesised $Pr_{2-x-y}Sr_{x+y}(Ni_{1-x}Co_x)O_{4\pm\delta}$, $y = 0.0$–0.75 ($x = 0.25$); $y = 0.0$–0.5 ($x = 0.5$) where the oxidation state of Ni has been varied by partial replacement of Pr^{3+} by Sr^{2+}. Effects of cations substitutions on the crystal structure, high-temperature electrical conductivity in air and thermal expansion behaviour of the novel compounds were investigated.

Experimental

$Pr_{2-x}Sr_xNi_{1-x}Co_xO_{4\pm\delta}$ ($x = 0.25$; 0.5; 0.75; 1.0) and $Pr_{2-x-y}Sr_{x+y}(Ni_{1-x}Co_x)O_{4\pm\delta}$, $y = 0.0$–0.75 ($x = 0.25$); $y = 0.0$–0.5 ($x = 0.5$) samples were prepared by conventional solid-state route in air at 1300–1350 °C, 20–24 h with preliminary annealing and regrinding at 950 °C, 24 h. Pr_6O_{11}, $SrCO_3$, NiO and Co_3O_4 (all analytical grade) were used as initial reagents. The densities of the ceramic samples were measured by pycnometry.

Phase purity of the compounds was checked by X-ray powder diffraction (XRPD) recorded on Huber G670 Guinier diffractometer ($CuK_{\alpha 1}$ radiation, image foil detector). High-temperature X-ray powder diffraction (HT XRPD) data in air were collected by Bruker D8-Advance diffractometer ($CuK_{\alpha 1}$ radiation, LynxEye PSD) in reflection mode equipped with high-temperature camera XRK-900 (Anton Paar). Unit cell parameters were refined by Rietveld method using TOPAS-3 program package. Oxygen content of the single-phase samples was determined by iodometric titration.

The thermal expansion behaviour of the samples was monitored by Netzsch 402C dilatometer in air at 25–900 °C with the heating rate of 10 K min^{-1}. TG studies were performed in artificial air (20% O_2(g), 80% Ar(g)) from 25 to 900 °C with a heating rate of 10 K min^{-1} by Netzsch STA 449C thermoanalyser.

High-temperature electrical conductivity of ceramic samples was measured in air by a standard 4-probe method in the temperature range of 25–900 °C. The samples had the shape of a disk with ~16–18 mm diameter and 1–2 mm thickness. The contacts were made from platinum wire ($d \sim 0.2$ mm) placed in alumina tube and were pressed independently to the surface of the sample by the separate individual springs situated at the top of the quartz sample holder kept at room temperature. The contacts were arranged in a line with 5–6 mm spacing between them. The influence of undesirable thermoelectric power was omitted by subtracting two successive voltage values on the potential contacts (the inner pair) measured at opposite current directions. The resulting resistivity value was recalculated into specific resistance using the approach developed in ref. 20.

Neutron powder diffraction data were collected using the POLARIS diffractometer at the ISIS pulsed spallation neutron source, Rutherford Appleton Laboratory, UK. Approximately 3 g of sample were loaded into a thin-walled cylindrical vanadium can and mounted in an automatic sample changer. Prior to analysis, the data were normalized using an incoherent scattering pattern from a vanadium sample. Structural models were tested by refinement of the neutron diffraction data using GSAS program package.[21]

High-temperature neutron diffraction (HT NPD) data were collected using high-resolution Fourier powder diffractometer (HRFD)[22] at IBR-2 pulsed reactor in Dubna (Russia). Rietveld

analysis of the data was performed using MRIA program package.[23] Data were collected at room temperature and at 100–500 °C in air with a step 100 °C.

High-temperature magnetic susceptibility measurements were performed on pressed pellets of $Pr_{2-x}Sr_xNi_{1-x}Co_xO_{4\pm\delta}$ (x = 0.0, 0.25; 0.5; 0.75) in the temperature range 10–800 K in applied magnetic fields up to 8 T using Quantum Design PPMS equipped with a vibrating sample magnetometer (VSM) option and oven setup. The measurements above 400 K were performed in high vacuum under constant gas pressure of 10^{-5} Torr. The samples were stable under these conditions, as confirmed by the excellent reproducibility of the data obtained during heating and cooling sweeps.

Results and discussion

$Pr_{2-x}Sr_xNi_{1-x}Co_xO_{4\pm\delta}$ (x = 0.25; 0.5; 0.75; 1.0)

Crystal structure. XRPD patterns of $Pr_{2-x}Sr_xNi_{1-x}Co_xO_{4\pm\delta}$ (x = 0.25; 0.5; 0.75; 1.0) samples were fully indexed in tetragonal unit cells (Table 1) showing the formation of oxides with K_2NiF_4-type structure. This is not surprising since orthorhombic $Pr_2NiO_{4+\delta}$ is known to transform to tetragonal phase for $x > 0.2$ in $Pr_{2-x}Sr_xNiO_{4\pm\delta}$.[7] Despite the larger ionic radius of Sr^{2+} in comparison with that of Pr^{3+} (rSr^{2+} = 1.31 Å, rPr^{3+} = 1.179 Å, CN = 9 (ref. 24)), both unit cell parameters decreased upon increasing the cobalt content due to the significantly smaller ionic radius of Co^{3+} in comparison with that of Ni^{2+} (rCo_{LS}^{3+} = 0.545 Å and rCo_{HS}^{3+} = 0.61 Å, rNi^{2+} = 0.69 Å). Iodometric titration revealed a decrease in the amount of hyperstoichiometric oxygen (δ) with increasing of cobalt content (Table 1) and for the $x = 0.5$ composition only a slight excess of oxygen is observed. This corresponds to the literature data for $Pr_{2-x}Sr_xNiO_{4\pm\delta}$,[8] where the composition with $\delta \approx 0.0$ is observed at $x = 0.5$. The average oxidation state of (Co/Ni) cations calculated from iodometric titration data expectedly increases with increasing x. Taking into account known from the literature stability of the oxidation state +3 for Co and Ni cations in perovskites, one can propose that Co cations are in oxidation state +3 only, while Ni cations are in mixed oxidation state between +2 and +3. It is notably that the Ni^{2+}-content also increases with increasing x due to the decrease of the hyperstoichiometric oxygen content. As it is known from literature, the oxygen content of undoped praseodymium nickelate corresponds to the chemical formula $Pr_2NiO_{4.22}$,[8] *i.e.* it contains 56% of Ni^{2+}. Assuming that all cobalt cations in $Pr_{2-x}Sr_xNi_{1-x}Co_xO_{4\pm\delta}$ are in the oxidation state +3, the calculated fraction of Ni^{2+} is ~70% in the $x = 0.25$ phase and ~100% in the $x = 0.75$ one.

Table 1 Unit cell parameters and oxygen content derived from iodometric titration results for $Pr_{2-x}Sr_xNi_{1-x}Co_xO_{4\pm\delta}$ (x = 0.25; 0.5; 0.75; 1.0)

x	a (Å)	c (Å)	Oxygen content ($4 \pm \delta$)	B-Cation oxidation state
0.25	3.8171(2)	12.3838(8)	4.11(1)	+2.47(2)
0.50	3.8049(1)	12.3201(6)	4.05(3)	+2.60(6)
0.75	3.7947(1)	12.3171(5)	3.99(2)	+2.73(4)
1.0	3.7787(2)	12.3415(7)	3.97(2)	+2.94(4)

Crystal structures of the x = 0.25 and 0.75 phases were refined using neutron powder diffraction data collected at room temperature. No reflection splitting was observed in both diffraction patterns, thus confirming the tetragonal crystal structure with S.G. *I*4/*mmm*. Reflections from admixtures of CoO and NiO were observed in NPD patterns of both compounds. However, their refined content was too small to have significant influence on the structure refinement. The refined weight fractions of NiO and CoO in the $x = 0.25$ sample were 0.0090(2) and 0.0035(5), and for x = 0.75–0.0029(2) and 0.0033(6), respectively. Observed, calculated, and difference NPD patterns for the $x = 0.25$ sample are given on Fig. S1.†

Crystal structure refinement for the $x = 0.25$ phase shows the presence of additional oxygen atoms positioned in the tetrahedral voids within the rock-salt slab (site O3 at 4d (0, 1/2, 1/4), Fig. 1). The oxygen content of the $x = 0.25$ phase calculated from the refined occupancy of this oxygen position (Table S1†) corresponds to $Pr_{1.75}Sr_{0.25}Ni_{0.75}Co_{0.25}O_{4.09\pm0.02}$ in excellent agreement with the results from the iodometric titration. No additional oxygen atoms were found at the 4d site in the crystal structure of $x = 0.75$ phase, in accordance with chemical titration results (Table 1). Selected interatomic distances in the crystal structures of $x = 0.25$ and 0.75 phases are given in Table S2.† Anisotropic atomic displacement parameters (ADP) for all atoms, except for O3, were used for the refinement of the crystal structures. Atomic displacement ellipsoids in the crystal structure of the $x = 0.25$ phase are shown in Fig. S2.† Substantial anisotropy of the oxygen atoms ADPs was observed in the crystal structure of the $x = 0.25$ phase. U_{33} for the equatorial oxygen atom O1 and U_{11} for the axial oxygen atom O2 are several times higher in comparison with those in the $x = 0.75$ phase (Table S1†). The most plausible explanation for such behaviour is the influence of the additional oxygen atom in the O3 position of the crystal structure for $x = 0.25$.

High-temperature thermal expansion behaviour. The high-temperature thermal expansion behaviour of the prepared phases was studied by both dilatometry and HT XRPD. Dilatometric curves for the $x = 0.25$, 0.5, 0.75 and 1.0 ceramic samples in air are shown in Fig. 2. All samples expand non-linearly with an accelerated expansion above ~550 °C. It should be mentioned that the corresponding TG-curves showed very little or no weight loss. Therefore, the observed non-linearity cannot be driven by the variation of the oxygen content with temperature (chemical expansion).

Large discrepancy between the values of TEC calculated from dilatometry data and from HT XRPD is observed for studied compounds (Table 2). This is especially the case for compositions with $x \geq 0.5$ containing large amounts of Co. The difference between the TEC values determined by dilatometry and HT HRPD approaches ~60% for the $x = 0.75$ sample. Such situation is very similar to what was observed and discussed in ref. 25, where the discrepancy was attributed to the large anisotropy of the thermal expansion along the *a*- and *c*-axes of the crystal structure. In this case large thermal stress of the ceramic sample is relaxed by the presence of internal micro cracks.

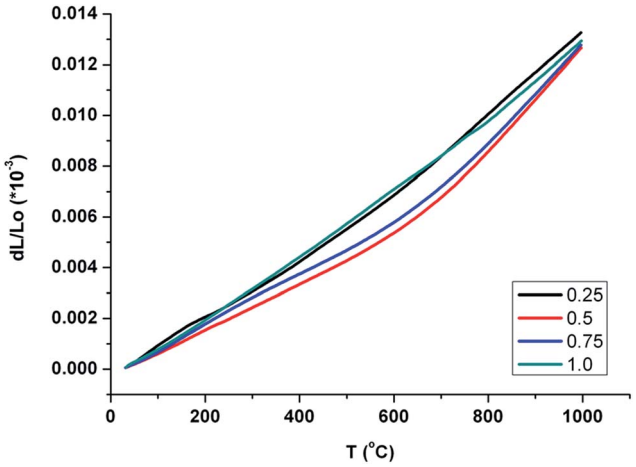

Fig. 2 Thermal expansion curves for $Pr_{2-x}Sr_xNi_{1-x}Co_xO_{4\pm\delta}$ (x = 0.25, 0.50, 0.75, 1.0) measured in air.

Table 2 TEC (ppm K^{-1}) at 25–850 °C calculated from HT XRPD and dilatometry (TEC_{dil}) for $Pr_{2-x}Sr_xNi_{1-x}Co_xO_{4\pm\delta}$ (x = 0.25, 0.50, 0.75, 1.0)

x	TEC(a)	TEC(c)	TEC(c)/TEC(a)	TEC ($V^{1/3}$)	TEC_{dil}
0.25	11.3	27.3	2.4	16.5	14.1
0.50	9.7	40.1	4.1	19.3	13.1
0.75	10.9	46.4	4.3	22.1	13.7
1.0	14.1	44.9	3.2	24.2	13.3

High-temperature crystal structure and magnetic properties. In order to obtain accurate values of the A– and B–O interatomic distances at various temperatures, HT NPD data were collected using the HRFD diffractometer for the x = 0.75 phase. Temperature dependence of the normalized unit cell parameters derived from HT NPD data is presented in Fig. 3. Linear temperature dependence of the a-parameter is observed in the whole studied temperature range, while the c-parameter shows non-linear dependence with much higher expansion rate.

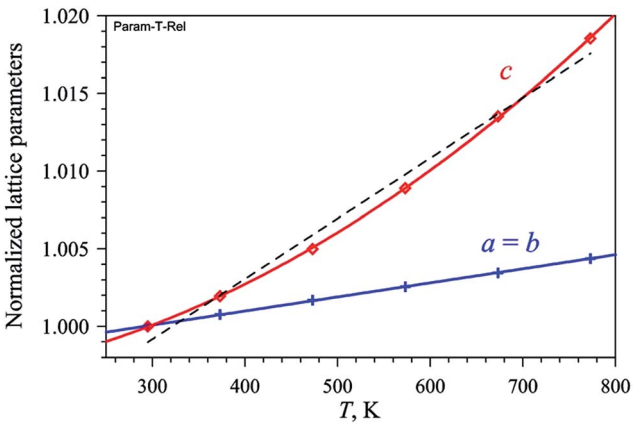

Fig. 3 Temperature dependence of the unit cell parameters for x = 0.75 phase derived from HT NPD data collected using HRFD diffractometer. Unit cell parameters were normalized by the unit cell parameter values at 295 K. Dashed line shows a linear fit of the c-parameter.

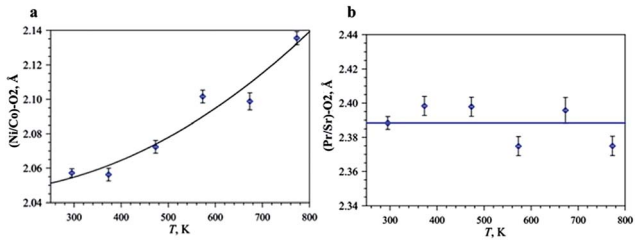

Fig. 4 Temperature dependence of the (Ni/Co)–O2 (a) and (Pr/Sr)–O2 (b) interatomic distances.

The expansion of (Ni/Co)–O2 and (Pr/Sr)–O2 bonds gives the highest contribution to the thermal expansion along the c-axis (Fig. 1). The temperature dependence of the (Ni/Co)–O2 interatomic distances is shown in Fig. 4a. TEC calculated for the expansion of axial (Ni/Co)–O2 bonds in studied temperature range is 75.7 ppm K^{-1}, while it is 9.1 ppm K^{-1} for the equatorial (Ni/Co)–O1 one. Therefore, a major contribution to the large expansion along the c-axis in the x = 0.75 phase is given by the expansion of the axial (Ni/Co)–O2 bond, whereas nearly no change of the (Pr/Sr)–O2 bond with temperature is observed (Fig. 4b). This situation is very similar to previous reports for $La_{2-x}Sr_xCoO_4$ (ref. 26) and $Pr_{1.25}Sr_{0.75}Cu_{0.25}Co_{0.75}O_{3.95(2)}$.[25] It was proposed that a temperature-induced transition between low- and high-spin states of Co^{3+} is responsible for such behaviour.

We were able to confirm this scenario by high-temperature magnetization measurements on a series of $Pr_{2-x}Sr_xNi_{1-x}Co_xO_{4\pm\delta}$ samples (Fig. 5). All of the samples revealed paramagnetic-like behaviour with no appreciable field dependence. The linear part of the inverse susceptibility was fitted by the Curie–Weiss law $\chi = C/(T+\theta)$, where $C = N_A\mu_{eff}^2/3k_B$ is the Curie constant yielding the paramagnetic effective moment μ_{eff}, and θ is the Curie–Weiss temperature. The fitted parameters are listed in Table 3 along with expected spin-only values, where we assumed Pr^{3+} (3.58 μ_B), Ni^{2+} (2.83 μ_B), and high-spin Ni^{3+} (3.87 μ_B) with the Ni^{2+}/Ni^{3+} ratio fixed by the oxygen stoichiometry. For Co-doped samples, both low-spin (0 μ_B) and high-spin (4.90 μ_B) regimes of Co^{3+} were considered.

The x = 0 sample revealed an effective moment of 6.24 μ_B per f.u. that can be understood as a combination of two Pr^{3+} ions and a mixture of Ni^{2+}/Ni^{3+} yielding μ_{eff} = 6.06 μ_B. The much lower effective moment of the x = 0.25 sample (μ_{eff} = 5.23 μ_B per f.u.) reflects the substitution of Pr^{3+} by non-magnetic Sr^{2+} and of Ni^{2+}/Ni^{3+} by non-magnetic low-spin Co^{3+}.

The high-temperature behaviour of the x = 0.5 and 0.75 samples is more complex. Here, one can identify two linear regions. Below 300–350 K, $1/\chi$ reveals effective moments, which are even lower than in the x = 0.25 sample and can be accounted by assuming that only Pr^{3+} and the residual Ni^{2+} are magnetic. Above 500 K, another linear region is observed, where the effective moment is around 6 μ_B and the Curie–Weiss temperature is much higher than at low temperatures. Both

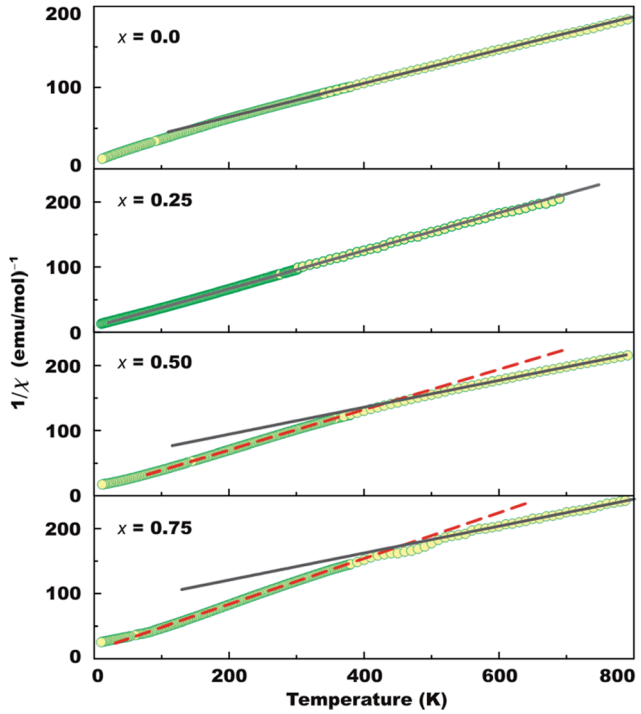

Fig. 5 Inverse magnetic susceptibility ($1/\chi$) of the samples with x = 0.0, 0.25, 0.50, and 0.75 measured in the applied field of 0.5 T. Lines are Curie–Weiss fits to the data yielding the parameters listed in Table 5.

Table 3 Paramagnetic effective moments μ_{eff} (per f.u.) and Curie–Weiss temperatures θ from linear fits of the inverse magnetic susceptibility. The calculated values of the effective moments are obtained assuming Pr^{3+} (3.58 μ_B), Ni^{2+} (2.83 μ_B), and high-spin Ni^{3+} (3.87 μ_B). For the x = 0.5 and 0.75 samples, the two values refer to the low-temperature (<500 K) and high-temperature (>500 K) regions, where non-magnetic (low-spin, 0 μ_B) and magnetic (high-spin, 4.90 μ_B) states of Co^{3+} are assumed, respectively

x	μ_{eff} (experiment), μ_B	μ_{eff} (calculated), μ_B	θ, K
0.00	6.24	6.06	111
0.25	5.23	5.47	29
0.50	5.08/6.21	4.89/5.99	26/253
0.75	4.76/6.21	4.25/6.00	37/382

observations suggest that at high temperatures Co^{3+} becomes magnetic, thus triggering strong interactions within the octahedral layers, while at low temperatures magnetic interactions measured by the Curie–Weiss temperature θ are on the order of 40–50 K and characteristic of the weak 4f magnetism.

These results show that the anomalously high expansion of the (Ni,Co)–O2 axial bond can be explained by a temperature-induced transition between low- and high-spin states of Co^{3+} which occurs at T > 500 K for the x = 0.5 and 0.75 phases. High-temperature NPD study shows that the calculated linear TEC of the (Ni,Co)–O2 axial bond for the x = 0.75 phase is 55 ppm K^{-1} in the temperature range 295–473 K and 87 ppm K^{-1} at 473–773 K.

Altogether we can conclude that high anisotropy of the thermal expansion of $Pr_{2-x}Sr_xNi_{1-x}Co_xO_{4\pm\delta}$ oxides with high Co-content ($x \geq 0.5$) hampers their use in high-temperature electrochemical devices since accumulation of the thermal stresses may results in their crumbling upon thermal cycling. For the phase with low Co-content ($x = 0.25$) another drawback was revealed. As mentioned above, one of the disadvantages of undoped $Pr_2NiO_{4+\delta}$ is its instability in oxygen at T > 850 °C, where it decomposes into $Pr_4Ni_3O_{10}$ and Pr_6O_{11}.[10,27,28] The treatment of the $x = 0.25$ phase in oxygen flow at 900 °C for 24 h revealed the partial oxidation into Pr_6O_{11} and $PrNiO_3$. In order to improve properties of $Pr_{2-x}Sr_xNi_{1-x}Co_xO_{4\pm\delta}$ oxides with low Co-content we prepared solid solutions $Pr_{2-x-y}Sr_{x+y}(Ni_{1-x}Co_x)O_{4\pm\delta}$, y = 0.0–0.75 (x = 0.25); y = 0.0–0.5 (x = 0.5) where we further increased the average oxidation state of Ni toward +3.

$Pr_{2-x-y}Sr_{x+y}(Ni_{1-x}Co_x)O_{4\pm\delta}$, y = 0.0–0.75 (x = 0.25); y = 0.0–0.5 (x = 0.5)

Crystal structure. Variation of the unit cell parameters of $Pr_{2-x-y}Sr_{x+y}(Ni_{1-x}Co_x)O_{4\pm\delta}$, y = 0.0–0.75 (x = 0.25); y = 0.0–0.5 (x = 0.5) *versus* Sr content is shown on Fig. 6. It is worth noting that the *a*-parameter for compositions with the same amount of Sr is smaller for the $x = 0.25$ series than for the $x = 0.5$ series for all Sr dopings, except for $PrSrNi_{1-x}Co_xO_{4\pm\delta}$. For the *c*-parameter, a different trend takes place, where, again with the exception of $PrSrNi_{1-x}Co_xO_{4\pm\delta}$, the *c*-parameter is higher for the $x = 0.25$ series than for the $x = 0.5$ series. One can consider spin and oxidation states of Co and Ni cations in these compounds. For example, for $Pr_{1.5}Sr_{0.5}Ni_{0.75}Co_{0.25}O_{4\pm\delta}$ and $Pr_{1.5}Sr_{0.5}Ni_{0.5}Co_{0.5}O_{4\pm\delta}$, considering their very similar, close to stoichiometric oxygen content ($\delta = 0.0$), the nominal oxidation state of B-cation is +2.5. It means that in $Pr_{1.5}Sr_{0.5}Ni_{0.5}Co_{0.5}O_4$ all cobalt and nickel cations are in the +3 and +2 oxidation states, respectively. Taking into account that cobalt is most likely in the oxidation state of +3, the chemical formula of $Pr_{1.5}Sr_{0.5}Ni_{0.75}Co_{0.25}O_{4\pm\delta}$ can be re-written as $Pr_{1.5}Sr_{0.5}Ni_{0.5}^{2+}Co_{0.25}^{3+}Ni_{0.25}^{3+}O_{4\pm\delta}$. Since the ionic radii of Co^{3+} (r_{LS} = 0.545 Å, r_{HS} = 0.61 Å) and Ni^{3+} (r_{LS} = 0.56 Å, r_{HS} = 0.60 Å) are very similar for the LS and HS states, one can speculate that Ni^{3+} is in the LS state in $Pr_{1.5}Sr_{0.5}Ni_{0.75}Co_{0.25}O_{4\pm\delta}$ and at least part of Co^{3+} is in the HS state in $Pr_{1.5}Sr_{0.5}Ni_{0.5}Co_{0.5}O_{4\pm\delta}$. This is because only such a combination results in the decrease of the ionic radius of the

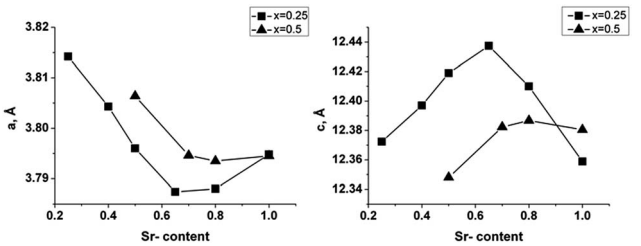

Fig. 6 Unit cell parameters *a* (left) and *c* (right) *versus* Sr content $Pr_{2-x-y}Sr_{x+y}(Ni_{1-x}Co_x)O_{4\pm\delta}$, y = 0.0–0.75 (x = 0.25); y = 0.0–0.5 (x = 0.5). The error values of the unit cell parameters are smaller that the symbols of the data points.

B-cation (and *a*-parameter) with increasing nickel content. It should be noted that LS Ni^{3+} ($t_{2g}^6e_g^1$) is a Jahn–Teller cation for which an axial elongation of the octahedron is expected. This explains the larger *c*-parameter for the $x = 0.25$ series in comparison with the $x = 0.5$ one. The presence of LS Ni^{3+} is observed in other nickelates like $RNiO_3$.[29]

A bell-like dependence of the *c*-parameter over Sr-content with the maximum at $y = 0.4$ ($Pr_{1.35}Sr_{0.65}Ni_{0.75}Co_{0.25}O_{4+\delta}$) is clearly observed for the $x = 0.25$ series, while it is less pronounced for the $x = 0.5$ series with a maximum at $y = 0.3$ ($Pr_{1.2}Sr_{0.8}Ni_{0.5}Co_{0.5}O_{4\pm\delta}$) (Fig. 6). At the same time, the *a*-parameter shows minimum for these compositions. Such a behaviour was also reported in the literature for the hole-doped nickelates $R_{2-x}Sr_xNiO_{4\pm\delta}$, R = La, Pr and Nd and can be explained by the transformation from $t_{2g}^6(z^2)^1$ to $t_{2g}^6(x^2-y^2)^1$ electron configuration of Ni^{3+}.[30]

For further studies we selected $Pr_{1.75-y}Sr_{0.25+y}Ni_{0.75}Co_{0.25}O_{4\pm\delta}$ compositions since Ni-rich oxide ($y = 0.0$) shows lowest TEC value (Table 2). Iodometric titration of the composition with the maximum *c*-axis ($Pr_{1.35}Sr_{0.65}Ni_{0.75}Co_{0.25}O_{4\pm\delta}$) showed the formation of a nearly oxygen stoichiometric phase with the oxygen content $(4 + \delta) = 4.01(2)$.

Thermal expansion behaviour and chemical stability of $Pr_{1.75-y}Sr_{0.25+y}(Ni_{0.75}Co_{0.25})O_{4\pm\delta}$. Thermal expansion behaviour of $Pr_{1.75-y}Sr_{0.25+y}(Ni_{0.75}Co_{0.25})O_{4\pm\delta}$, $y = 0.25$, 0.4, 0.55 and 0.75 was studied by both dilatometry and HT XRPD. The results are summarized in Table 4. Similar to the $Pr_{2-x}Sr_xNi_{1-x}Co_xO_{4\pm\delta}$ samples (Table 2), a rather large anisotropy of the thermal expansion along the *a*- and *c*-axes accompanied by the discrepancy between the TEC values calculated from HT XRPD data and dilatometry data is observed. The TEC values for the ceramic samples are rather low and comparable with those for typical electrolytes in IT-SOFC like 20GDC (12.8 ppm K^{-1})[31] or LSGM2020 (12.8 ppm K^{-1}).[32]

For $Pr_{1.35}Sr_{0.65}Ni_{0.75}Co_{0.25}O_{4\pm\delta}$ ($y = 0.40$) both chemical stability in oxygen atmosphere and toward chemical interaction with standard electrolyte materials for SOFC like GDC and YSZ were studied. In comparison with $Pr_{1.75}Sr_{0.25}Ni_{0.75}Co_{0.25}O_{4\pm\delta}$ phase ($y = 0.0$), no decomposition was observed after heat treatment in oxygen gas flow at 900 °C for 24 h. It should be noted that both unit cell parameters and oxygen content remained unchanged during such treatment. The higher stability of the $y = 0.40$ sample in oxygen is most likely related to the higher oxidation state of nickel cations (+2.56 assuming Co^{3+} and Pr^{3+}) in comparison with +2.29 in the $y = 0.0$ sample, which prevents further oxidation of nickel.

For the stability test towards chemical interaction with GDC and YSZ, powder of $Pr_{1.35}Sr_{0.65}Ni_{0.75}Co_{0.25}O_{4\pm\delta}$ was mixed with electrolytes in 1 : 1 mass ratios and annealed at 800–1100 °C with a step of 100 °C during 50 h. An XRPD study revealed vigorous reactivity with YSZ, which started already at 900 °C with the formation of $Pr_2Zr_2O_7$ and $SrZrO_3$ (see Fig. S3a†). However, no admixture phases were observed after heating $Pr_{1.35}Sr_{0.65}Ni_{0.75}Co_{0.25}O_{4\pm\delta}$/GDC mixture up to 1200 °C (see Fig. S3b†). Therefore, $Pr_{1.35}Sr_{0.65}Ni_{0.75}Co_{0.25}O_{4\pm\delta}$ oxide may be used as cathode either with GDC electrolyte directly or with the YSZ electrolyte separated by the protective layer of GDC.

High-temperature electrical conductivity of $Pr_{1.75-y}Sr_{0.25+y}(Ni_{0.75}Co_{0.25})O_{4\pm\delta}$, $y = 0.0$, $y = 0.15$ and 0.40. High-temperature electrical conductivity measurements were performed in air at 25–1000 °C (Fig. 7). The data were satisfactorily fitted by Arrhenius-like law modified for small polarons hopping:

$$\sigma(T) = \frac{A}{T}\exp\left(-\frac{E_a}{kT}\right), \quad (1)$$

where T is the absolute temperature, k – Boltzmann's constant, A – a pre-exponential factor, E_a – the activation energy. Values of E_a are given in Table 5 together with electrical conductivity values at 700 °C and 900 °C.

Owing to the substantially different porosity of the samples (Table 5), we recalculated electrical conductivity values taking the porosity into account using the formula from ref. 33:

$$\sigma_{cor} = \sigma_{exp}\frac{1 + p/2}{(1-p)^{2/3}}, \quad (2)$$

where p is the porosity and σ_{exp} and σ_{cor} are the electrical conductivities measured experimentally and corrected for porosity, respectively. An increase in the electrical conductivity with Sr-doping is observed for the samples with a highest conductivity at around 300 S cm^{-1} at 700 °C for the $y = 0.4$

Table 4 TEC (ppm K^{-1}) at 25–850 °C calculated from HT XRPD and dilatometry (TEC_{dil}) for $Pr_{1.75-y}Sr_{0.25+y}(Ni_{0.75}Co_{0.25})O_{4\pm\delta}$

y	TEC(a)	TEC(c)	TEC(c)/TEC(a)	TEC ($V^{1/3}$)	TEC_{dil}
0.25	—	—	—	—	13.0
0.4	11.2[a]	27.9	2.4	16.8	13.0
0.55	—	—	—	—	12.1
0.75	10.0	28.2	2.8	16.1	—

[a] Average TEC value at 25–850 °C. Two temperature ranges for the expansion along *a*-axis with TEC = 9.5 ppm K^{-1} (25–400 °C) and TEC = 12.9 ppm K^{-1} are observed.

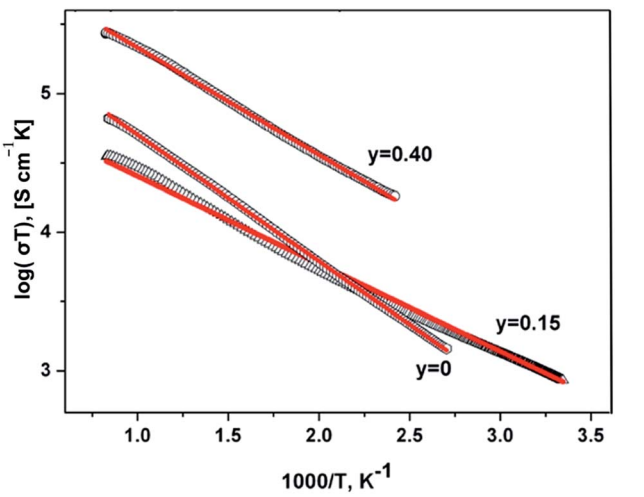

Fig. 7 Temperature dependence of electrical conductivity for $Pr_{1.75-y}Sr_{0.25+y}(Ni_{0.75}Co_{0.25})O_{4\pm\delta}$, $y = 0.0$, $y = 0.15$ and 0.40. Red lines show fit of the experimental data according to eqn (1), while black symbols are experimental points.

Table 5 Experimental high-temperature electrical conductivity values (σ_{exp}, S cm^{-1}) and those corrected for porosity (σ_{cor}, S cm^{-1}) at 700 °C and 900 °C for $Pr_{1.75-y}Sr_{0.25+y}(Ni_{0.75}Co_{0.25})O_{4\pm\delta}$, $y = 0.0$, $y = 0.15$ and 0.40 ceramic samples

y	σ_{exp}, 700 °C	σ_{exp}, 900 °C	σ_{cor}, 700 °C	σ_{cor}, 900 °C	E_a, eV	Density, %
0.0	43	56	61	80	0.18	72
0.15	28	30	50	54	0.13	56
0.40	260	280	293	315	0.15	90

sample. An increase in the electrical conductivity with Sr-content was also observed for $Pr_{2-x}Sr_xNiO_{4\pm\delta}$,[33,34] although the values of the electrical conductivity are significantly lower, with the reported maximum of 138.5 S cm^{-1} at 600 °C for $x = 0.8$.[34] It should be mentioned that, in comparison with the $Pr_{1.75-y}Sr_{0.25+y}(Ni_{0.75}Co_{0.25})O_{4\pm\delta}$ samples, $Pr_{2-x}Sr_xNiO_{4\pm\delta}$ demonstrate a decrease in the electrical conductivity with temperature, *i.e.*, a metallic-like behaviour.[33,34]

Conclusions

By simultaneous replacement of Ni for Co and Pr for Sr in $Pr_2NiO_{4+\delta}$ we have successfully prepared $Pr_{2-x}Sr_xNi_{1-x}Co_xO_{4\pm\delta}$ (x = 0.25; 0.5; 0.75) oxides with the tetragonal K_2NiF_4-type structure. Similar to other Co-containing oxides with the K_2NiF_4-type structure, $Pr_{2-x}Sr_xNi_{1-x}Co_xO_{4\pm\delta}$ (x = 0.25; 0.5; 0.75) show substantial anisotropy of the thermal expansion along the *a*- and *c*-axes of the crystal structure, and this anisotropy increases upon Co substitution. This results in a rather large difference between the TEC values calculated from dilatometry and HT XRPD data. Using a combination of HT NPD and HT magnetization measurements, we showed for the first time that such anisotropy of thermal expansion is most likely associated with the temperature-induced transition between low- and high-spin states of Co^{3+} cations.

In order to further vary the oxidation state of Ni in $Pr_{2-x}Sr_xNi_{1-x}Co_xO_{4\pm\delta}$, $x = 0.25$ and 0.5 oxides, we replaced Pr^{3+} by Sr^{2+}. This allowed to prepare $Pr_{1.35}Sr_{0.65}Ni_{0.75}Co_{0.25}O_{4\pm\delta}$ composition with very promising properties as cathode material in IT-SOFC. This material shows the TEC of 13.0 ppm K^{-1} comparable with that of GDC electrolyte, as well as the chemical stability in oxygen at 900 °C as well as towards interaction with GDC up to 1250 °C. This composition exhibits high values of high-temperature electrical conductivity in air approaching 300 S cm^{-1} at 900 °C and is considered as promising cathode material in IT-SOFC.

Acknowledgements

This work was partially supported by Russian Foundation for Basic Research (grants no. 14-03-01083, 14-29-04091 ofi_m), by Skolkovo Institute of Science and Technology (Center of Electrochemical Energy) and MSU-development Program up to 2020. AAT acknowledges partial financial support by the Federal Ministry of Science and Education through the Sofja Kovalevskaya Award of Alexander von Humboldt Foundation.

Notes and references

1 E. Boehm, J.-M. Bassat, P. Dordor, F. Mauvy, J.-C. Grenier and P. Stevens, *Solid State Ionics*, 2005, **176**, 2717.
2 J. D. Sullivan, D. J. Buttrey, D. E. Cox and J. Hriljac, *J. Solid State Chem.*, 1991, **94**, 337.
3 R. Saez Puche, F. Fernández, J. Rodríguez Carvajal and J. L. Martínez, *Solid State Commun.*, 1989, **72**, 273.
4 H. Tamura, A. Hayashi and Y. Ueda, *Phys. C*, 1996, **258**, 61.
5 Y. Toyosumi, H. Ishikawa and K. Ishikawa, *J. Alloys Compd.*, 2006, **408–412**, 1200.
6 E. Niwa, K. Wakai, T. Hori, K. Yashiro, J. Mizusaki and T. Hashimoto, *Thermochim. Acta*, 2014, **575**, 129.
7 S. C. Chen, K. V. Ramanujachary and M. Greenblatt, *J. Solid State Chem.*, 1993, **105**, 444.
8 C. Allançon, P. Odier, J. M. Bassat and J. P. Loup, *J. Solid State Chem.*, 1997, **131**, 167.
9 A. Chroneos, D. Parfitt, J. A. Kilner and R. W. Grimes, *J. Mater. Chem.*, 2010, **20**, 266.
10 P. Odier, C. Allanion and J.-M. Bassat, *J. Solid State Chem.*, 2000, **153**, 381.
11 J. E. Millburn, M. A. Green, D. A. Neumann and M. J. Rosseinsky, *J. Solid State Chem.*, 1999, **145**, 401.
12 Y. Takeda, M. Nishijima, N. Imanishi, R. Kanno, O. Yamamoto and M. Takano, *J. Solid State Chem.*, 1992, **96**, 72.
13 Y. Takeda, R. Kanno, M. Sakano, O. Yamamoto, M. Takano, Y. Bando, H. Akinaga, K. Takita and J. B. Goodenough, *Mater. Res. Bull.*, 1990, **25**, 293.
14 M. J. Sayagues, M. Vallet-Regi, A. Caneiro and J. M. Gonzalez-Calbet, *Solid State Ionics*, 1993, **66**, 21–26.
15 A. Aguadero, M. J. Escudero, M. Perez, J. A. Alonso, V. Pomjakushin and L. Daza, *Dalton Trans.*, 2006, 4377.
16 J. Yang, J. Cheng, Q. Jiang, Y. Wang, R. Wang and J. Gao, *Int. J. Hydrogen Energy*, 2012, **37**, 1746.
17 V. Vashook, J. Zosel, T.-L. Wen and U. Guth, *Solid State Ionics*, 2006, **177**, 1827.
18 S. J. Skinner and J. A. Kilner, *Solid State Ionics*, 2000, **135**, 709.
19 T. Inprasit, S. Wongkasemjit, S. J. Skinner, M. Burriel and P. Limthongkul, *RSC Adv.*, 2015, **5**, 2486.
20 H. R. Kokabi, J. Provost and G. Desgardin, *Rev. Sci. Instrum.*, 1993, **64**, 1549.
21 A. C. Larson and R. B. Von Dreele, General Structure Analysis System (GSAS), Los Alamos National Laboratory Report LA-UR-86-748, 2000, B. H. Toby, "EXPGUI, a graphical user interface for GSAS", *J. Appl. Crystallogr.*, 2001, **34**, 210.
22 A. M. Balagurov, *J. Neutron Res.*, 2005, **16**, 8.
23 V. B. Zlokazov and V. V. Chernyshev, *J. Appl. Crystallogr.*, 1992, **25**, 447.
24 R. D. Shannon, *Acta Crystallogr., Sect. A: Cryst. Phys., Diffr., Theor. Gen. Crystallogr.*, 1976, **32**, 751.
25 G. N. Mazo, S. M. Kazakov, L. M. Kolchina, A. V. Morozov, S. Y. Istomin, N. V. Lyskov, A. A. Gippius and E. V. Antipov, *J. Alloys Compd.*, 2015, **639**, 381.

26 C. Tealdi, C. Ferrara, L. Malavasi, P. Mustarelli, C. Ritter, G. Chiodelli and Y. Diaz-Fernandez, *Phys. Rev. B: Condens. Matter Mater. Phys.*, 2010, **8**, 174118.
27 F. Mauvy, C. Lalanne, J.-M. Bassat, J.-C. Grenier, H. Zhao, L. Huo and P. Stevens, *J. Electrochem. Soc.*, 2006, **153**, A1547.
28 A. Montenegro-Hernandez, J. Vega-Castillo, L. Mogni and A. Caneiro, *Int. J. Hydrogen Energy*, 2011, **36**, 15704.
29 M. L. Medarde, *J. Phys.: Condens. Matter*, 1997, **9**, 1679.
30 J. Gopalakrishnan, G. Colsmann and B. Reuter, *J. Solid State Chem.*, 1977, **22**, 145.
31 F. Tietz, *Ionics*, 1999, **5**, 129.
32 J. W. Stevenson, T. R. Armstrong, L. R. Pederson, J. Li, C. A. Levinsohn and S. Baskaran, *Solid State Ionics*, 1998, **113–115**, 571.
33 V. Vashook, J. Zosel, T.-L. Wen and U. Guth, *Solid State Ionics*, 2006, **177**, 1827.
34 J. Yang, J. Cheng, Q. Jiang, Y. Wang, R. Wang and J. Gao, *Int. J. Hydrogen Energy*, 2012, **37**, 1746.

